JASA ARTICLE

Dynamically orthogonal narrow-angle parabolic equations for stochastic underwater sound propagation. Part II: Applications

Wael H. Ali[1,2] and Pierre F. J. Lermusiaux[1,2,a)]

[1]Department of Mechanical Engineering, Massachusetts Institute of Technology, Cambridge, Massachusetts 02139, USA

[2]Center for Computational Science and Engineering, Massachusetts Institute of Technology, Cambridge, Massachusetts 02139, USA

ABSTRACT:

The stochastic dynamically orthogonal (DO) narrow-angle parabolic equations (NAPEs) are exemplified and their properties and capabilities are described using three new two-dimensional stochastic range-independent and range-dependent test cases with uncertain sound speed field, bathymetry, and source location. We validate results against ground-truth deterministic analytical solutions and direct Monte Carlo (MC) predictions of acoustic pressure and transmission loss fields. We verify the stochastic convergence and computational advantages of the DO-NAPEs and discuss the differences with normal mode approaches. Results show that a single DO-NAPE simulation can accurately predict stochastic range-dependent acoustic fields and their non-Gaussian probability distributions, with computational savings of several orders of magnitude when compared to direct MC methods. With their coupling properties and their adaptation in range to the dominant uncertainties, the DO-NAPEs are shown to predict accurate statistics, from mean and variance to multiple modes and full probability distributions, and to provide excellent reconstructed realizations, from amplitudes and phases to other specific properties of complex realization fields.

 https://doi.org/10.1121/10.0024474

(Received 21 November 2023; revised 8 January 2024; accepted 8 January 2024; published online 25 January 2024)

[Editor: John A. Colosi] Pages: 656–672

I. INTRODUCTION

In Part I of this two-part paper (Ali and Lermusiaux, 2024), we derived, discretized, and implemented stochastic differential equations that (i) capture the dominant input uncertainties in the environment (e.g., ocean, bathymetry, and seabed) and in the acoustic parameters (e.g., source location, frequency, and bandwidth), and (ii) predict the acoustic pressure fields and their probability distributions, respecting the nonlinear governing equations and non-Gaussian statistics. Starting from the acoustic Parabolic Equation (PE), we derived Dynamically Orthogonal (DO) differential equations for range-optimal acoustic uncertainty quantification. Using DO expansions for the input uncertainties, we developed the reduced-order DO-PEs theory and applied it to derive the Dynamically Orthogonal Narrow-Angle Parabolic Equation (DO-NAPE) stochastic partial differential equations (PDEs).

In the present study, we illustrate and analyze the properties and capabilities of the DO-NAPEs in a wide range of test cases with varying sources of uncertainty and increasing complexity. We focus on stochastic acoustic propagation in two-dimensional (2D) space (depth z, range η; stochastic parameter ξ), within ocean environments with uncertain sound speed, bathymetry, and source depth. The goal is to predict the DO decomposition $\boldsymbol{\psi}_{DO}$ and TL_{DO} of the stochastic complex envelope pressure field $\boldsymbol{\psi}(z,\eta;\xi)$ and transmission loss $TL(z,\eta;\xi)$, respectively. The sources of uncertainties are the stochastic squared effective index of refraction $n^2_{eff}(z,\eta;\xi)$, stochastic bathymetry $b(\eta;\xi)$, and stochastic source depth $Z_s(\xi)$. The boundary conditions are assumed deterministic, as well as the source frequency and range. The relevant notation and the DO-NAPEs are provided in the Appendix for convenience.

The three new stochastic test cases are defined by extending existing deterministic test cases: (1) an uncertain range-independent Pekeris Waveguide (PW) with stochastic sound speed, (2) an uncertain range-independent Horizontal Interface (HI) problem with stochastic source depth, and (3) an uncertain range-dependent Up-sloping Wedge (UW) problem with stochastic bathymetry. All three test cases use a penetrable fluid bottom.

For each test case, a different source of uncertainty is considered. The results will showcase the advantages of the DO-NAPE over the state-of-the-art techniques in stochastic underwater sound propagation with non-Gaussian inputs. In particular, the stochastic PW case (Sec. II) features an uncertain water sound speed and is used to highlight DO-NAPE properties and complete convergence studies validating our results. The stochastic HI case (Sec. III) is based on an uncertain source depth and employs the DO-NAPE to predict the probability of TL fields. Last, the stochastic UW case (Sec. IV) has an uncertain bathymetry and is used to verify the accuracy of DO-NAPE in capturing the dominant

a)Email: pierrel@mit.edu

https://doi.org/10.1121/10.0024474

TABLE I. Simulation parameters for the three test cases: uncertain Pekeris Waveguide (PW) with a stochastic water sound speed $c_w(\xi)$, uncertain Horizontal Interface (HI) with a stochastic source depth $Z_s(\xi)$, and uncertain Up-sloping Wedge (UW) with a stochastic depth intersect $Z_w(\xi)$ at the final range. The symbol f denotes the source frequency, Z_{max} the medium depth (including the fluid bottom), dz the vertical finite volume cell size, R the total range, and $d\eta$ the range step size. Finally, n_{s,n^2} and $n_{s,\psi}$, introduced in Eq. (A3), are the sizes of the stochastic subspaces for the environment and acoustics, respectively, and n_r is the number of samples used to evolve the stochastic DO coefficients governed by the ODEs [Eq. (A4c)] as was described in Sec. III E 2 in the Part I paper (Ali and Lermusiaux, 2024).

Test case	Uncertainty type	f (Hz)	Z_{max} (m)	dz (m)	R (m)	$d\eta$ (m)	n_{s,n^2}	$n_{s,\psi}$	n_r
PW	$c_w \sim U[1470, 1520]$ m/s	250	300	1	10000	0.5	1	10	5000
HI	$Z_s \sim U[20, 180]$ m	100	900	1	10000	1	0	20	1000
UW	$Z_w \sim U[0, 200]$ m	25	1500	1	4000	1	6	9	2000

uncertainties efficiently in a range-dependent medium with large uncertainties.

The DO-NAPE solutions are validated against analytical solutions (PW case) and standard Monte Carlo (MC) techniques (HI and UW cases). For all the validation results where an MC ensemble is used, the approach of Ueckermann *et al.* (2013) is followed: each ensemble member is run using initial conditions (ICs), boundary conditions (BCs), and uncertainty sampling consistent with what is done for the DO-NAPE solution. The DO-NAPE properties are highlighted and their advantages are discussed with respect to other approaches such as Polynomial Chaos (PC) and random media methods (Ali and Lermusiaux, 2024).

The main simulation parameters for the three stochastic test cases are listed in Table I.

II. UNCERTAIN PEKERIS WAVEGUIDE (PW)

The first test case extends the deterministic PW with a penetrable fluid bottom (Jensen *et al.*, 2011; Pekeris, 1948) to a stochastic PW with a probabilistic water sound speed. In this 2D shallow water test case, a point sound source located at depth $Z_s = 25$ m and range $\eta = 0$ is emitting at a harmonic frequency $f = 250$ Hz. The waveguide is an isospeed sound channel with density $\rho_w = 1000\,\mathrm{kg/m^3}$ and no attenuation. The bottom consists of a fluid half-space with sound speed $c_b = 1590$ m/s, density $\rho_b = 1200\,\mathrm{kg/m^3}$, and attenuation $a_b = 0.5\,\mathrm{dB}/\lambda$. In its new stochastic extension, the waveguide environment is uncertain with a stochastic water sound speed c_w of uniform Probability Density Function (PDF), i.e., $c_w \sim U[1470, 1520]$ m/s. The reference sound speed is $c_0 = 1500$ m/s. A schematic of the test case is given in Fig. 1.

To illustrate the effect of the uncertain c_w, deterministic solutions for two sample sound speed values, $c_w = (1470, 1510)$ m/s, are provided. As the deterministic Pekeris waveguide admits an analytical solution using wavenumber integration (Jensen *et al.*, 2011; Pekeris, 1948; Schmidt and Jensen, 1985), the analytical solutions for the two sample sound speed values are shown in Fig. 2. The differences in the interference patterns between the two solutions are readily apparent by comparing the phase fields [Figs. 2(a) and 2(b)]. Both solutions retain common features of acoustic propagation in a lossy bottom Pekeris waveguide, in particular, the shadow zone around the range of 7 km as highlighted by the transmission loss field, $TL = -20\log_{10}\left(|\psi|/\sqrt{\eta}\right)$, shown in Figs. 2(c) and 2(d).

A. DO-NAPE solutions

The DO-NAPEs [Eq. (A4)] are forced by the DO decompositions of the effective squared index of refraction. Figure 3(a) shows the uncertain sound speed profiles $c(z;\xi)$, obtained by sampling uniformly $n_r = 5000$ realizations of $c_w \sim U[1470, 1520]$, as well as the corresponding realizations of $(c_0/c(z;\xi))^2$, and those of the effective squared index of refraction $n^2_{eff}(z;\xi)$ given by Eq. (A1). Using these realizations, the DO decomposition of $n^2_{eff}(z;\xi)$ is computed by singular value decomposition (SVD) and used as input to the DO-NAPEs. With this idealized test case (range-independent isospeed waveguide with a scalar uncertainty), only one DO mode is needed for n^2_{eff}. The mean profile $\overline{n^2}(z)$, DO mode profile $\widetilde{n^2}_1(z)$, and PDF of the DO coefficient β_1 are shown in Fig. 3(b). Due to the uniform distribution of the water sound speed, the marginal PDF of β_1 is also nearly uniform as expected (the slight discrepancy is due to sampling error and, only for the plot, to the normal kernel density fit that smoothes the edges.). They force the DO-NAPEs [Eq. (A4)].

Using the DO-NAPEs [Eq. (A4)] and the initialization procedure for deterministic source frequency and location described in case 2 of Sec. III E 3 of Part I (Ali and Lermusiaux, 2024), the DO decomposition of the stochastic acoustic pressure field is then predicted, with a subspace size $n_{s,\psi} = 10$ (see Table I for other DO-NAPE parameters). The range evolution of the magnitude of the complex-

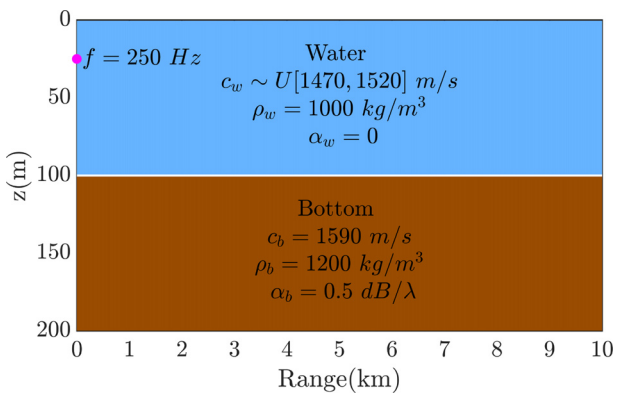

FIG. 1. (Color online) Uncertain PW: Schematic. A point sound source located at depth $Z_s = 25$ m and range $\eta = 0$ emits at a harmonic frequency $f = 250$ Hz. The water sound speed c_w is uncertain with a uniform PDF, i.e., $c_w \sim U[1470, 1520]$ m/s. Other parameters are deterministic as given in the schematic and described in the text.

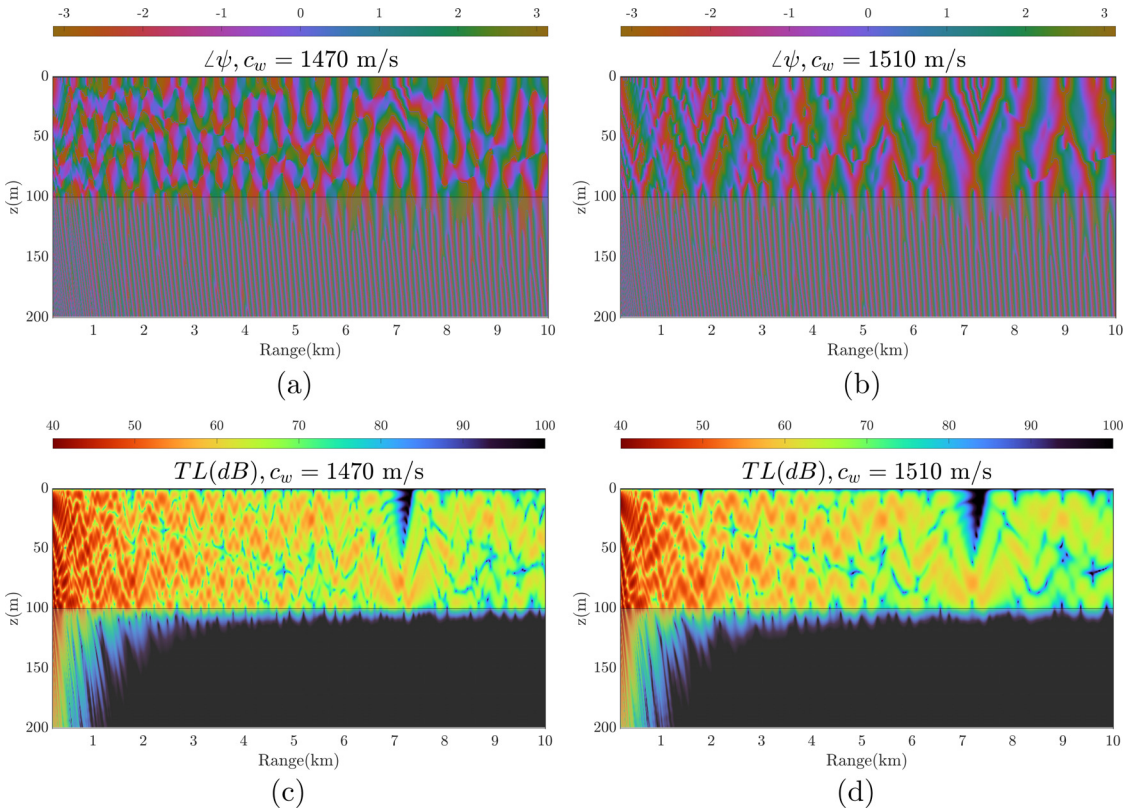

FIG. 2. (Color online) Uncertain PW: Analytical pressure solutions for two sample sound speed realizations, $c_w = (1470, 1510)$ m/s, obtained using wavenumber integration. (a) and (b) Phase fields (in radians) of the pressure envelope, and (c) and (d) transmission loss fields (in dB), for each sound speed value.

valued mean envelope function $|\bar{\psi}(z,\eta)|$ is shown in Fig. 4. Profiles of the mean solution at sample ranges $\eta = 0.5$, $2.5, 5, 7.5, 10$ km are shown in Figs. 4(a) and 4(b), and the full depth-range field in Fig. 4(c). Comparing the DO mean prediction to the deterministic solutions shown in Fig. 2, it is clear that the DO mean solution retains the common features, e.g., the shadow zone around 7 km in range and the significant attenuation in the bottom.

In addition to the mean field, the DO-NAPEs predict the DO modes and stochastic DO coefficients of the pressure solution. A convergence study (discussed in Sec. II B) was performed to determine the size $n_{s,\psi}$ of the stochastic subspace which resulted in choosing $n_{s,\psi} = 10$. Figure 5 shows the real parts of the dominant four (out of ten) modes and (range-dependent) coefficients. We highlight the highly non-Gaussian marginal PDFs at sample ranges $\eta = 0.5, 2.5$, $5, 7.5, 10$ km. The bimodality of the PDFs corresponds to the distinct acoustic physics when c_w is smaller or larger than the reference sound speed c_0.

Figure 6 shows the evolution of the principal variances $\sigma_i^2(\eta), i = 1, \ldots, n_{s,\psi}$, which provide a measure of the stochastic energy and its changes with range. The red curve

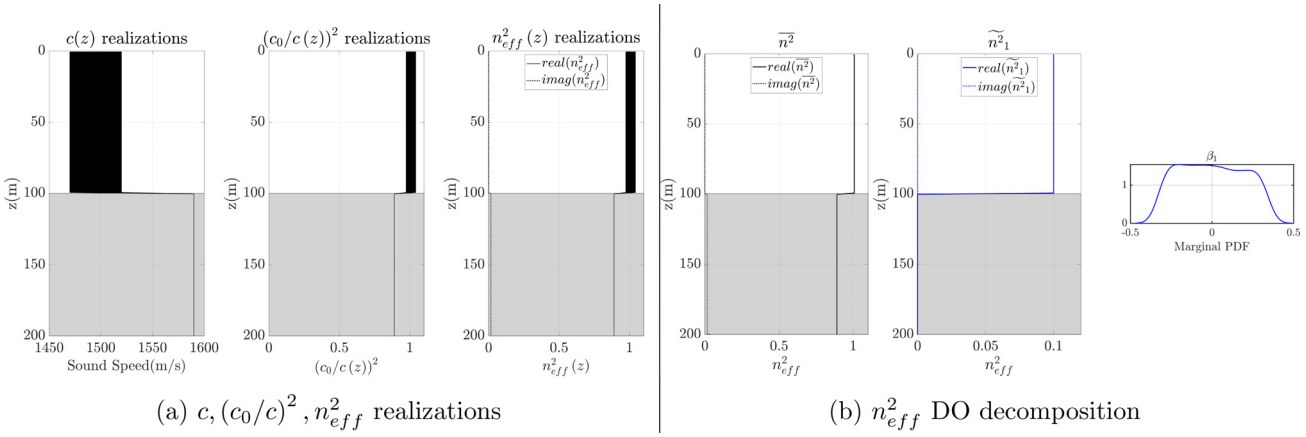

(a) $c, (c_0/c)^2, n^2_{eff}$ realizations (b) n^2_{eff} DO decomposition

FIG. 3. (Color online) Uncertain PW: Input realizations and decomposition. (a) Sound speed profile realizations with the corresponding realizations of $(c_0/c(z;\xi))^2$ and $n^2_{eff}(z;\xi)$. (b) Mean profile $\overline{n^2}(z)$, first DO mode profile $\widetilde{n^2}_1(z)$, and PDF of first DO coefficient β_1. The gray shading in all profile plots represents the fluid bottom medium.

https://doi.org/10.1121/10.0024474

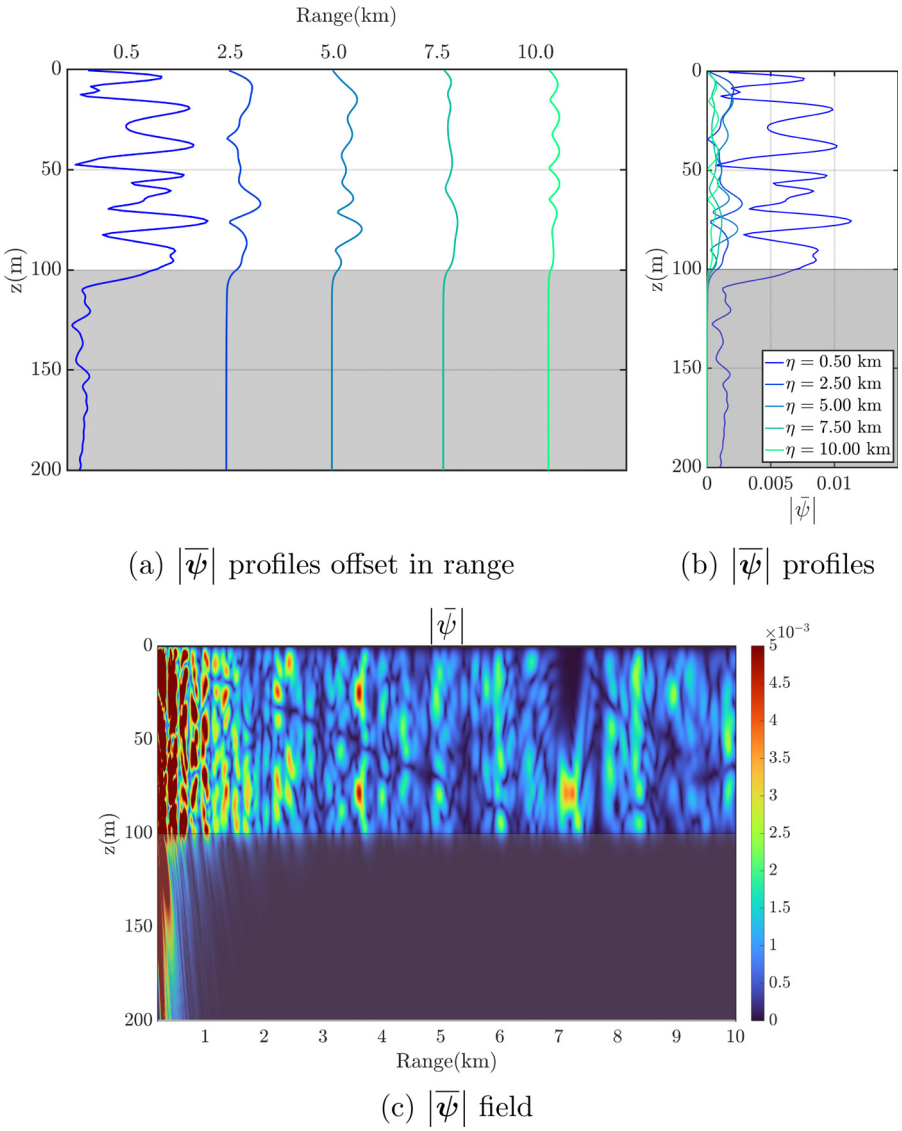

(a) $|\overline{\psi}|$ profiles offset in range

(b) $|\overline{\psi}|$ profiles

$|\bar{\psi}|$

(c) $|\overline{\psi}|$ field

FIG. 4. (Color online) Uncertain PW: DO-NAPE mean pressure solution $|\bar{\psi}|$ (in Pa). (a) and (b) Solution profiles shown at sample ranges $\eta = 0.5, 2.5, 5, 7.5, 10$ km. (c) Full solution field.

corresponds to the deterministic energy of the mean pressure, $\langle \bar{\psi}(\cdot,\eta), \bar{\psi}(\cdot,\eta) \rangle$. We observe that the stochastic energy is comparable to the mean energy, highlighting the strong and complex uncertainties in this idealized uncertain PW case.

Finally, using the cost ratio Eq. (A5), the computational cost of direct MC can be compared to that of DO-NAPE. Inserting the present parameters $\kappa = 1$, $n_r = 5000$, $n_{s,n^2} = 1$, and $n_{s,\psi} = 10$, we obtain a saving factor of $\text{Cost}_{MC}/\text{Cost}_{DO} \sim 250$.

B. Stochastic convergence analysis

To demonstrate the stochastic convergence of our DO-NAPE equations and schemes as $n_{s,\psi}$ and n_r are increased, an MC ensemble of analytical solutions obtained by uniformly sampling $n_r = 5000$ realizations of the water sound speed was computed and used as a reference solution. We note that this allows us to evaluate both the dynamic DO truncation errors and the DO numerical scheme errors.

Convergence with the stochastic subspace dimension. Figure 7 shows the MC mean field and compares it to the DO-NAPE mean field solutions as the size of stochastic subspace $n_{s,\psi}$ is increased. The relative differences $||\bar{\psi}_{DO}| - |\bar{\psi}_{MC}||/|\bar{\psi}_{MC}|$ are shown for $n_{s,\psi} = 2, 6, 8, 10$ [the DO-NAPE mean field with $n_{s,\psi} = 10$ was shown in Fig. 4(c)]. From the figure, it is found that the relative difference decreases significantly in the water medium when $n_{s,\psi}$ is augmented from 2 to 6 after which the DO solution in the bottom medium further approaches the MC solution as $n_{s,\psi}$ is increased to 10. The larger relative difference in the bottom towards the final ranges is due to the solution itself being very small (bottom attenuation and long ranges). Overall, comparing the mean solution from the MC ensemble of analytical solutions [Fig. 7(a)] and the DO-NAPE mean solution [Fig. 4(c)], it can be seen that the solutions are indistinguishable.

Convergence with the DO coefficient realizations sample size. The convergence of the DO-NAPE solution as the number of samples n_r increases is also examined. The results of this analysis are shown in Fig. 8, which displays the decay of the error for the mean solution compared to the MC solution [Fig. 8(a)] and the convergence in the marginal

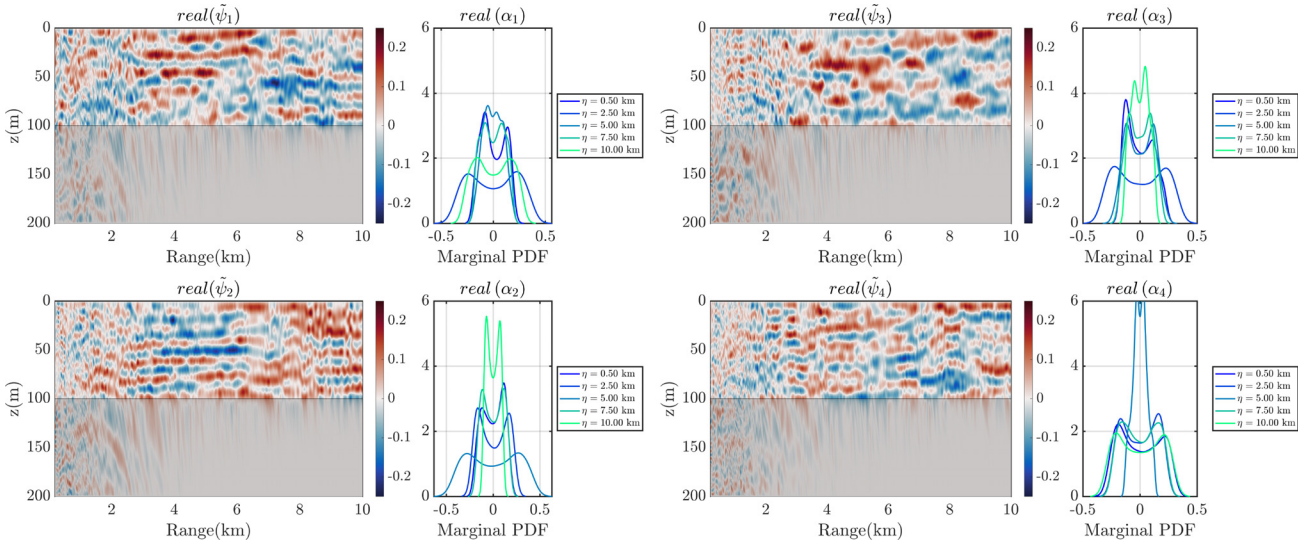

FIG. 5. (Color online) Uncertain PW: DO-NAPE stochastic modes (non-dimensional) and coefficients (in Pa) solutions. The real parts of the dominant four (out of ten) DO modes and coefficients are shown. The evolution of the DO modes with range is clear and the marginal PDFs of the DO coefficients, shown at sample ranges $\eta = 0.5, 2.5, 5, 7.5, 10$ km, highlight the non-Gaussian PDFs.

distribution of the four dominant stochastic coefficients (real parts of α_i, $i = 1, \ldots, 4$), at three sample ranges $\eta = 0.5$, 5, and 10 km [Fig. 8(b)]. As n_r is increased from 500 to 5000 (curves shown as decreased transparency in the color of the distributions for the three sample ranges), the bimodal range-dependendent PDFs of the coefficients converge.

C. DO-NAPE validation

To illustrate the validation of the DO solution, the analytical solutions shown in Fig. 2 are compared to the corresponding DO-NAPE solutions for the two sample sound speed realizations, $c_w = 1470$ and $c_w = 1510$ m/s. The latter DO pressure solutions are reconstructed once the full DO-NAPE solution is computed using the samples of the stochastic coefficients that correspond to the chosen sound speed realizations. In other words, denoting the two sample stochastic parameters corresponding to the chosen sound speed realizations by ξ_1 and ξ_2, the DO pressure solutions are reconstructed as

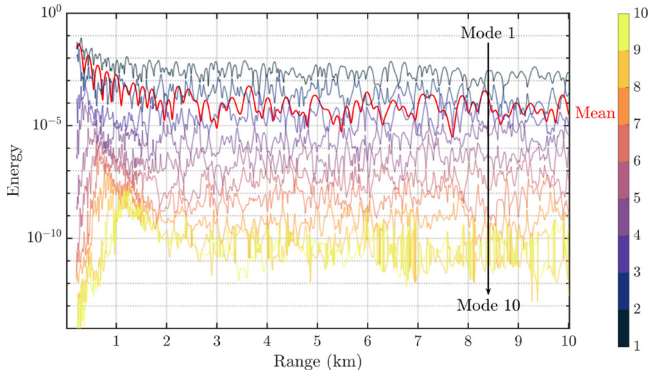

FIG. 6. (Color online) Uncertain PW: Evolution in range of the principal variances $\sigma_i^2(\eta), i = 1, \ldots, 10$, and of the mean pressure energy, $\langle \bar{\psi}(\cdot, \eta), \bar{\psi}(\cdot, \eta) \rangle$, shown in red (all in Pa^2).

$$\psi_{DO}(z, \eta; \xi_{1,2}) = \bar{\psi}(z, \eta) + \sum_{i=1}^{n_{s,\psi}} \tilde{\psi}_i(z, \eta) \alpha_i(\eta; \xi_{1,2}),$$

from which the DO phase and DO TL are computed.

These comparison results are shown in Fig. 9. The top two rows show the phase and TL realizations as a function of range at a receiver located at $Z_{receiver} = 50$ m for the two sound speed realizations, $c_w = 1470$ and $c_w = 1510$ m/s. The DO-NAPE solutions are shown for increasing dimensions of the stochastic subspace, $n_{s,\psi} = 2, 4, 6, 8, 10$. The subspace dimension $n_{s,\psi} = 10$ yields phase and TL results (shown in maroon red) that are in excellent agreement with the true analytical solutions (shown in red). The bottom two rows in Fig. 9 show the error in the phase ($\angle\psi_{analytical} - \angle\psi_{DO}$) and TL ($TL_{analytical} - TL_{DO}$) solutions computed using DO-NAPE with $n_{s,\psi} = 10$. We find that the DO-NAPE TL and phase solutions show excellent agreement, especially in the water medium. We note that many more comparisons were made than just these two realizations and the DO-NAPE accuracy remained excellent. The relatively larger discrepancies between the DO-NAPE and true solutions in the bottom medium can be mitigated by increasing the size of the stochastic subspace (results not shown). In this work, the focus is on the acoustic propagation in the water medium, and as a result, the agreement obtained using $n_{s,\psi} = 10$ is sufficient.

III. UNCERTAIN HORIZONTAL INTERFACE (HI)

The second test case extends the deterministic Horizontal Interface (HI) case, also known as the Bucker waveguide (Lee and McDaniel, 1988), to a stochastic HI case with a probabilistic source depth. A point sound source emits at a harmonic frequency $f = 100$ Hz in a shallow water domain. The uncertain depth of the sound source is

https://doi.org/10.1121/10.0024474

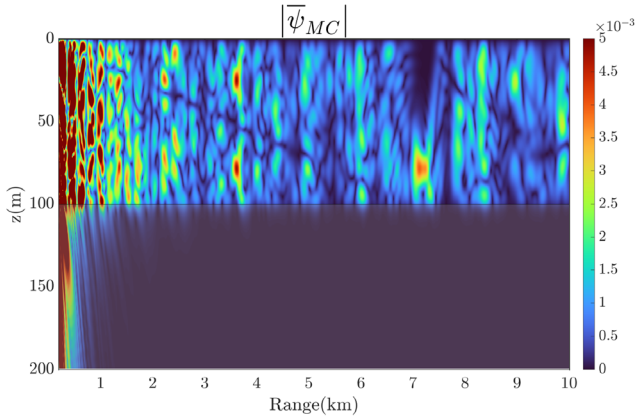

(a) MC mean solution

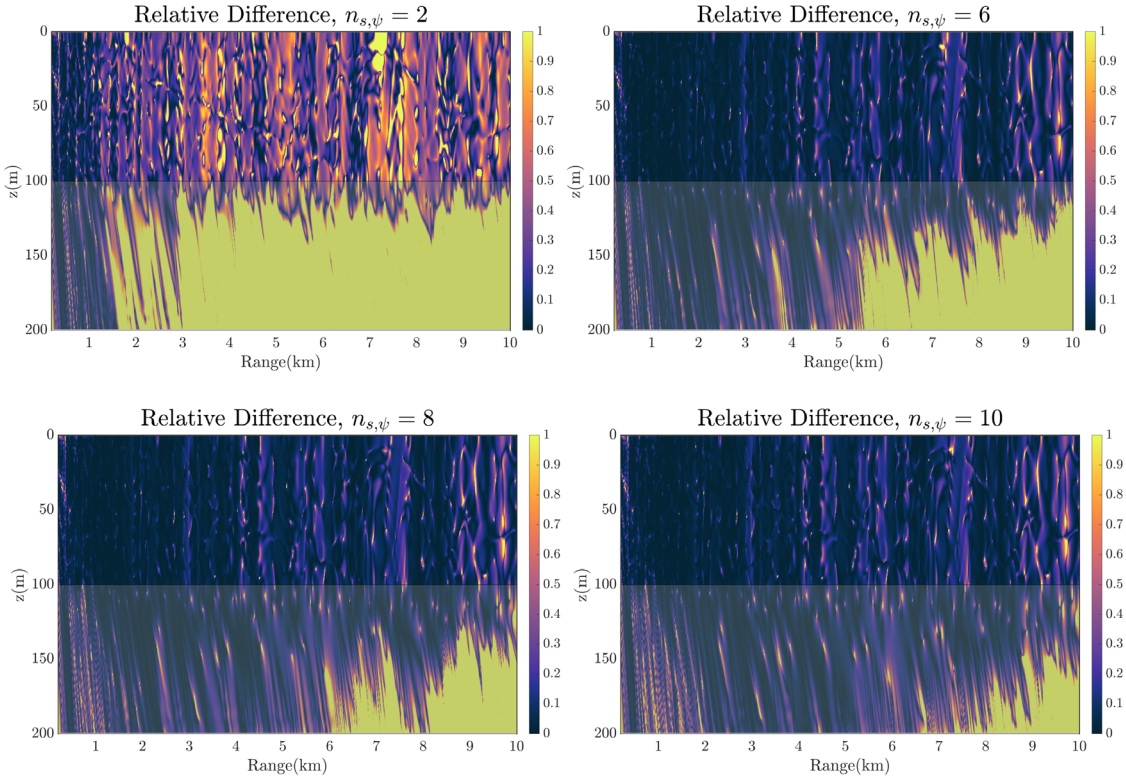

(b) Relative differences in the DO mean solutions

FIG. 7. (Color online) Uncertain PW: Convergence analysis of the DO-NAPE mean solution as the size of the stochastic subspace $n_{s,\psi}$ increases. (a) Mean solution (in Pa) obtained from an MC ensemble of analytical solutions of size 5000. (b) Relative differences between the DO-NAPE means for $n_{s,\psi} = 2, 6, 8, 10$, and the MC mean.

assumed to be a uniform random variable with $Z_s \sim U[20, 180]$ m. The deterministic waveguide is a piecewise linear sound speed profile that has a minimum value of 1498 m/s at 120 m depth, $\rho_w = 1000\,\mathrm{kg/m^3}$, and $\alpha_w = 0$. The seabed is a sediment layer with $c_s = 1550$ m/s, $\rho_s = 2100\,\mathrm{kg/m^3}$, and $\alpha_s = 0\,\mathrm{dB}/\lambda$. The bottom below the seabed is modeled as a fluid half-space with $c_b = 1600$ m/s, $\rho_b = 2200\,\mathrm{kg/m^3}$, and $\alpha_b = 1\,\mathrm{dB}/\lambda$. The reference sound speed is $c_0 = 1500$ m/s. A schematic of the test case is given in Fig. 10.

A. DO-NAPE initialization

Due to the uncertainties in the source depth, case 1 of the initialization procedure described in Sec. III E 3 of Part I (Ali and Lermusiaux, 2024) is used. By uniformly sampling $n_r = 1000$ realizations of the source depth $Z_s \sim U[20, 180]$ m, the stochastic Gaussian starter defined in Eq. (15) of Ali and Lermusiaux (2024) is used to generate realizations of the initial pressure field $\boldsymbol{\psi}^0(z; \xi)$. These realizations are shown in Fig. 11(a) along with their covariance heatmap.

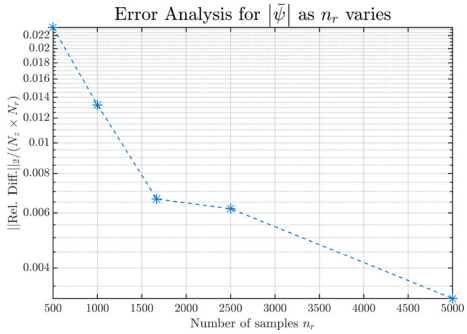

(a) Mean Convergence

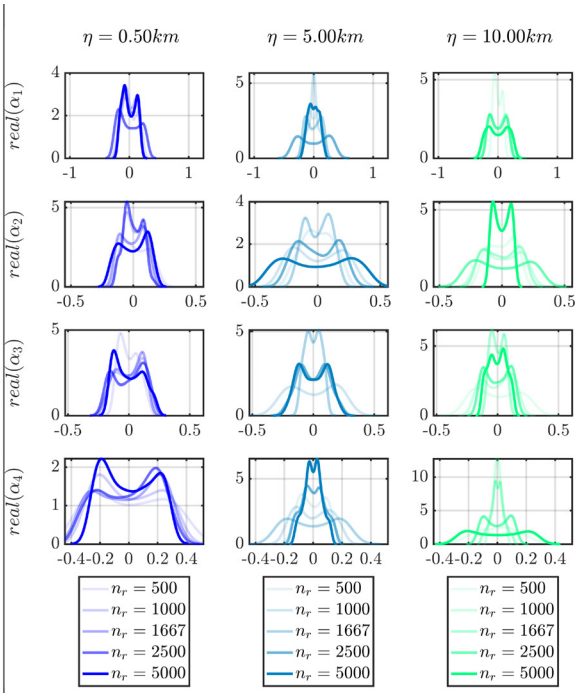

(b) Stochastic Coefficients Convergence

FIG. 8. (Color online) Uncertain PW: Convergence analysis of the DO-NAPE solution as the number of samples n_r is increased from 500 to 5000. (a) Mean field relative error as a function of n_r. (b) Real parts of the four dominant DO-NAPE coefficients (α_i, $i = 1, \ldots, 4$, in Pa) at the ranges $\eta = 0.5$, 5, and 10 km.

The source depth realizations are sampled independently resulting in a diagonal covariance matrix in the range $z \in [20, 180]$ m. The subspace size $n_{s,\psi}$ of the truncated SVD is chosen to be 20 in order to capture 99% of the variance in the starter realizations as shown in Fig. 11(b). From the truncated SVD, the ICs at $\eta = 0$ of the DO-NAPE mean $\bar{\psi}(z, \eta)$, modes $\widetilde{\psi}_{i=1,\ldots,20}(z, \eta)$, and coefficients $\alpha_{i=1,\ldots,20}(\eta; \xi)$ are computed. Figure 11(c) shows the profiles of the starter mean, modes $i = 1, 5, 10, 15, 20$, and the PDFs of their corresponding coefficients. Note that all profiles extend over the entire depth of the sediment and the bottom halfspace, down to $z = Z_{max} + D = 1200$ m, where $D = 300$ m is the thickness of the artificial absorption layer. However, the source depth uncertainties in this case only lead to non-zero mean and mode profiles for $z \in [20, 180]$ m. As the sound moves further in range, these uncertainties propagate to other depths as shown in the results next.

B. DO-NAPE ψ solutions

As the sound speed, density, and attenuation are assumed exactly known (deterministic), the stochastic NAPE [Eq. (A2)] for this case only contains uncertain initial conditions (source depth) and no stochastic forcing. The versatility of our DO-NAPE approach allows us to still use Eq. (A4) with all the uncertain n_{eff}^2 terms null. A convergence study (as shown in Fig. 11) was also used to choose the size of the stochastic pressure subspace, $n_{s,\psi} = 20$, and it will be illustrated in Fig. 14.

The DO-NAPE mean solution as well as the two most dominant and the least dominant stochastic DO modes and coefficients are shown in Fig. 12. Comparing the most and least dominant stochastic modes, larger scale uncertainty features (especially in the water medium) are captured by the dominant modes 1 and 2, while the least dominant mode 20 captures smaller scale uncertainties. The DO-NAPE solution predicts the variance explained at each sample range: e.g., for modes 1, 2, and 20, at $\eta = 0.5$ km: $Var(\alpha_1) = 0.0949, Var(\alpha_2) = 0.0931, Var(\alpha_{20}) = 0.0097$; at $\eta = 5$ km: $Var(\alpha_1) = 0.137, Var(\alpha_2) = 0.121, Var(\alpha_{20}) = 1.05 \times 10^{-4}$; and at $\eta = 10$ km: $Var(\alpha_1) = 0.0847, Var(\alpha_2) = 0.0834$, $Var(\alpha_{20}) = 3.81 \times 10^{-7}$ (Pa^2). The highly non-Gaussian and range-dependent distributions of these stochastic coefficients showcase some of the advantages of DO-NAPE compared to other PC-based schemes. Such range dependence makes PC-based schemes more computationally expensive or less accurate due to their fixed polynomial basis (Branicki and Majda, 2013). For similar accuracy, much more terms in the PC expansion would need to be used, at all ranges. In comparison to MC, for this test case, using $\kappa = 1$, $n_r = 1000$, and $n_{s,\psi} = 20$ in the cost ratio Eq. (A5), one obtains $\text{Cost}_{MC}/\text{Cost}_{DO} \sim 50$, which highlights the computational advantage of the DO-NAPE framework.

As discussed in Sec. IV of Part I (Ali and Lermusiaux, 2024), the DO-PEs exhibit fundamental differences from normal mode schemes, especially from their simplifications such as the adiabatic approximation. The fully coupled property of DO modes, missing from the adiabatic normal mode approximation, can be illustrated using the HI case discussed herein. Although the DO mean and modes had no signature in the bottom halfspace at the initial range (Fig. 11), the DO subspace at later ranges allows for both

https://doi.org/10.1121/10.0024474

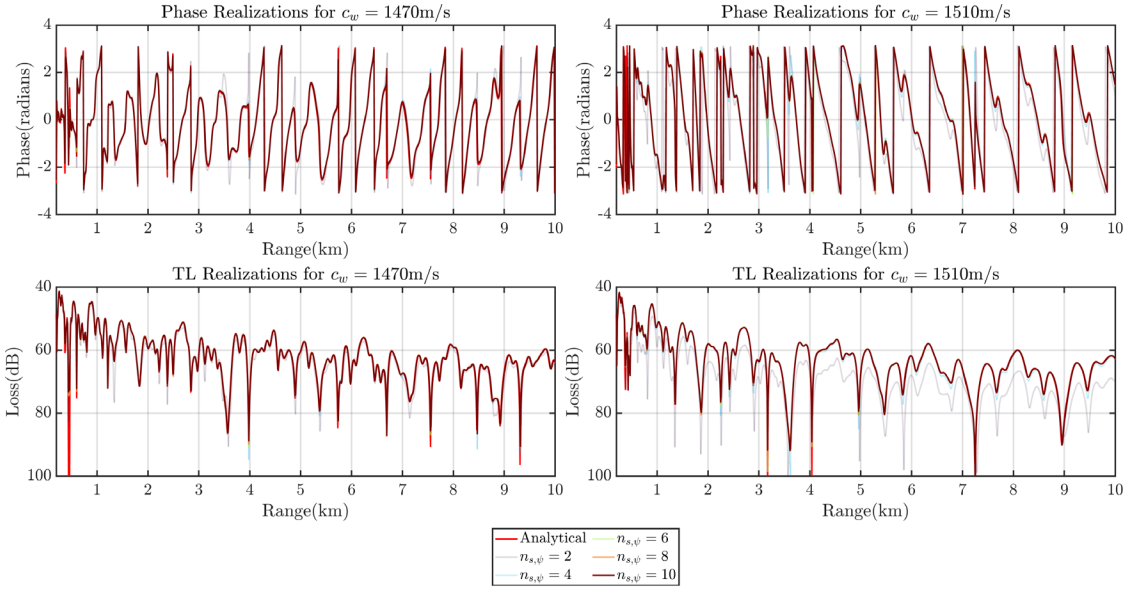

(a) Phase and TL realizations at $Z_{receiver} = 50\ m$

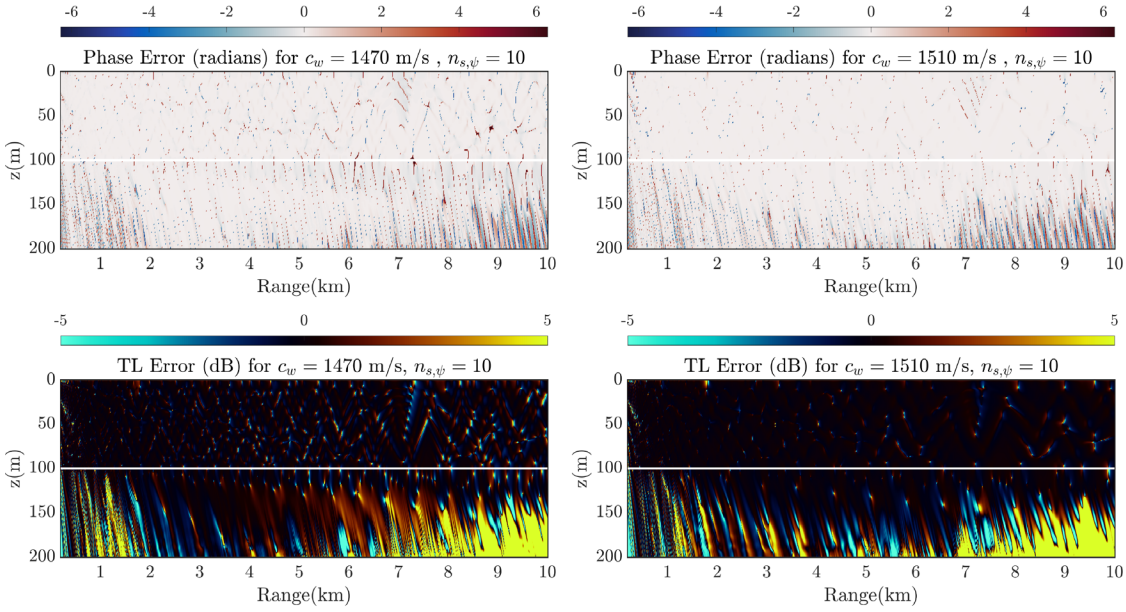

(b) Phase and TL Errors

FIG. 9. (Color online) Uncertain PW: Comparisons of the phase (in radians) and TL (in dB) computed by DO-NAPE to the corresponding analytical solutions, for two sample realizations of water sound speed: $c_w = 1470$ m/s (first column), and $c_w = 1510$ m/s (second column).

the mean and modes to be nonzero there (Fig. 12): the stochastic acoustic field is indeed transmitted to the bottom when the solution is marched in range.

C. DO-NAPE TL solutions

Starting from the DO-NAPE ψ solution, the global SVD of TL described in Sec. III G of Part I (Ali and Lermusiaux, 2024) and summarized in the Appendix is used to compute the statistics and reconstruct sample realizations of TL. The DO-NAPE TL results are validated using the ensemble of 1000 MC runs. Comparisons between the DO and MC solutions for the mean and standard deviation of TL are shown in Fig. 13. The DO-NAPE TL solutions show excellent agreement. In particular, comparing the mean fields, the maximum relative error in the water is found to be ≈2% and that in the bottom was ≈5%. For the standard deviations, the maximum relative errors are found to be ≈3% in the water and ≈6.5% in the bottom.

In addition to matching the first- and second-order statistics of TL, the DO-NAPE TL solutions are validated by performing realization-based comparisons for 3 sample

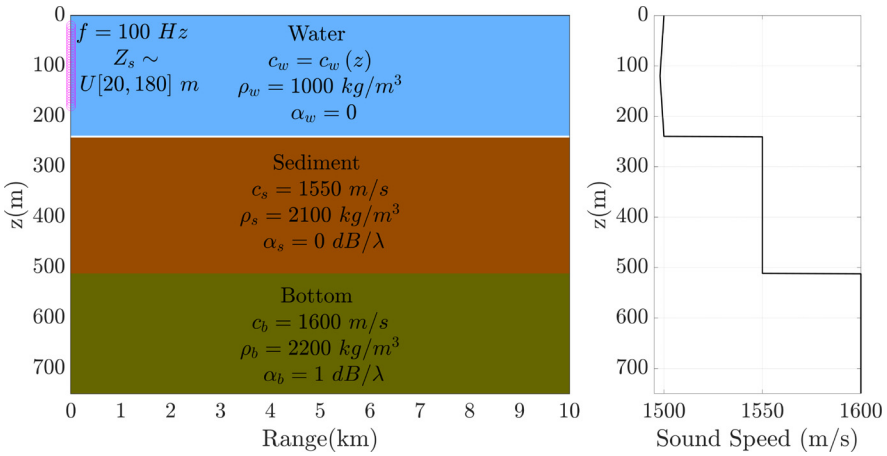

FIG. 10. (Color online) Uncertain HI: Schematic. A point sound source emits at a harmonic frequency $f = 100$ Hz in a shallow water domain. The depth of the source is uncertain with a uniform PDF, i.e., the random variable $Z_s \sim U[20, 180]$ m. Other parameters are deterministic as given in the schematic and described in the text.

source depths: $Z_s = 20, 100, 180$ m. The TL comparisons at two receiver locations, $Z_{receiver} = 30, 190$ m, are shown in Fig. 14. As the size of the stochastic subspace $n_{s,\psi}$ increases, the DO-NAPE TL solutions, computed at a much lower computational cost than a brute force MC method, tend to the MC solution (shown in red). As expected, the error increases slightly for longer ranges due to the fixed dimension of each stochastic subspace and the accumulation of the corresponding truncation errors. To address this, one can adapt the stochastic subspace dimension for longer ranges,

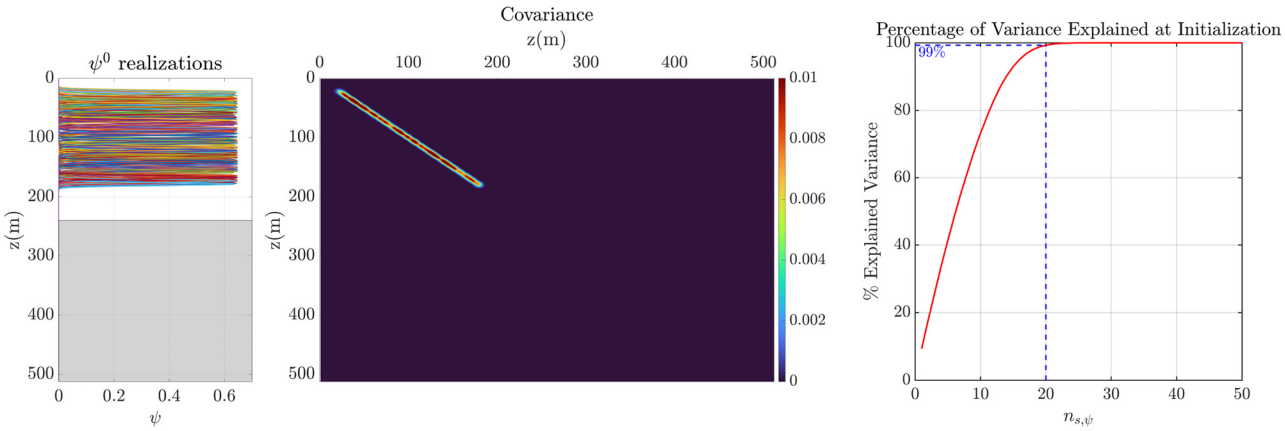

(a) ψ^0 realizations and covariance (b) % of explained variance

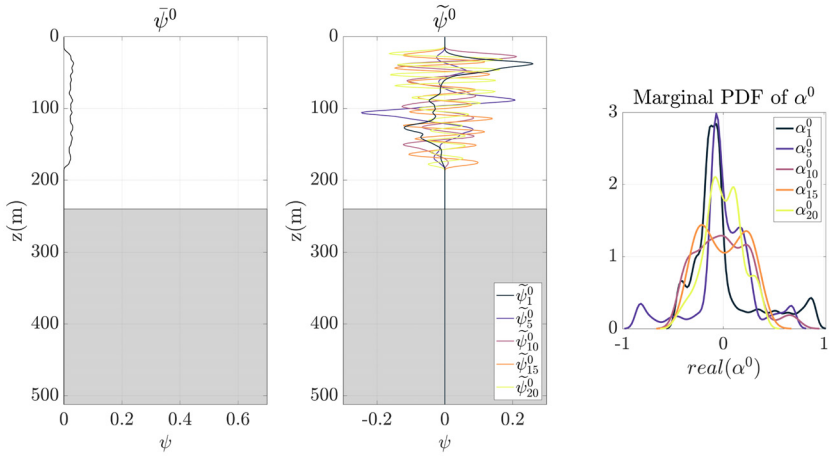

(c) ψ^0 DO decomposition

FIG. 11. (Color online) Uncertain HI: DO-NAPE Initialization. (a) Realizations (in Pa) and covariance (in Pa^2) of the starter realizations $\psi^0(z;\xi)$. (b) Percentage of variance in the stochastic Gaussian starter realizations explained by the truncated SVD, along with the choice of subspace size $n_{s,\psi} = 20$ to capture 99% of the variance. (c) DO-NAPE initial conditions for the mean $\bar{\psi}^0(z)$ (in Pa), 5 (out of the 20) modes $\tilde{\psi}^0(z)$, and PDF of the corresponding DO coefficients $\alpha^0(\xi)$. The gray shading in all profile plots represents the fluid sediment medium. The bottom halfspace is omitted as the starter field vanishes there by construction.

https://doi.org/10.1121/10.0024474

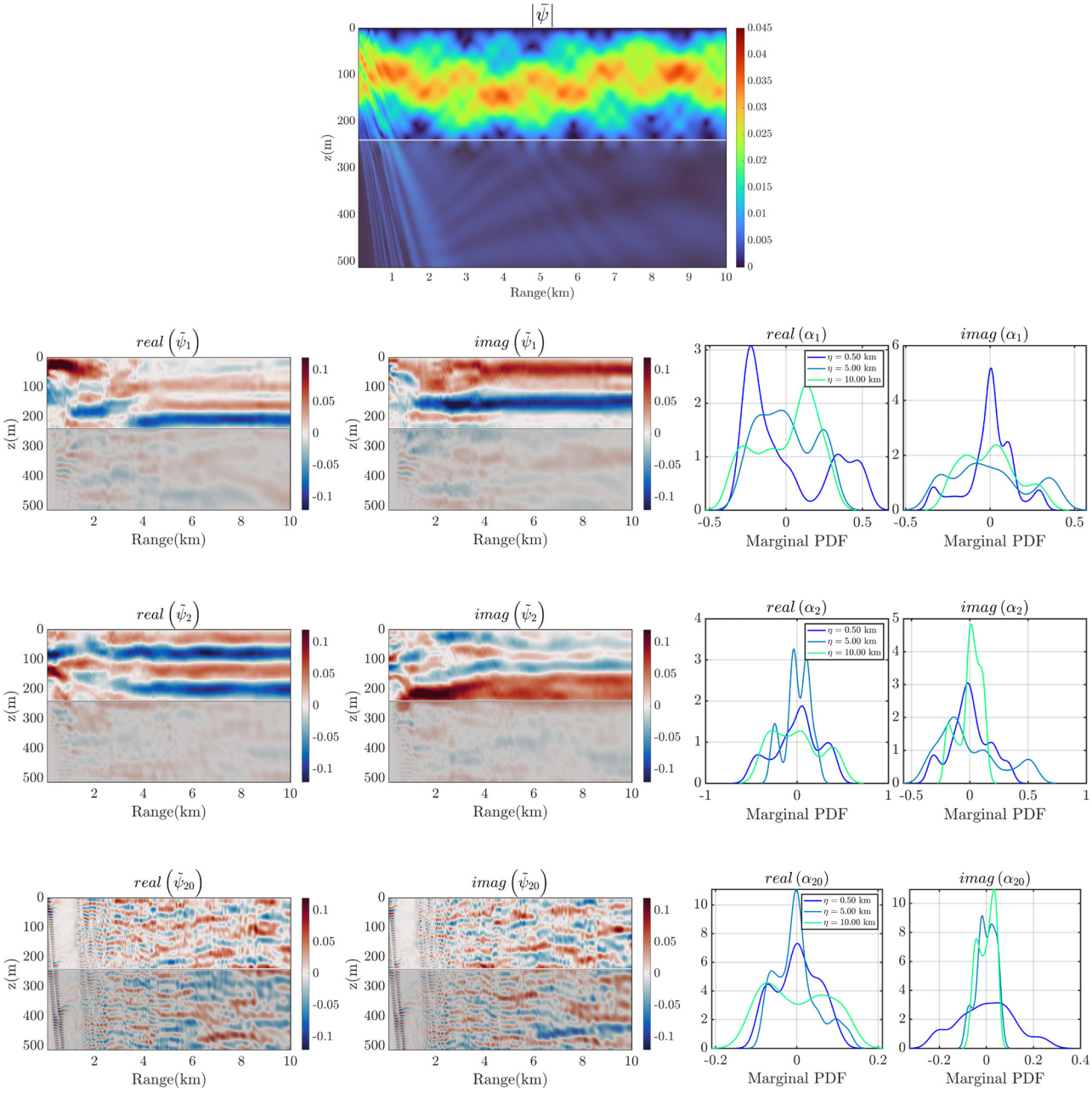

FIG. 12. (Color online) Uncertain HI: DO-NAPE mean (in Pa), modes (non-dimensional), and coefficients (in Pa) solutions. The magnitude of the mean solution is shown in the top panel. The real and imaginary parts of the two most dominant modes 1 and 2 and of the least dominant mode 20 are shown, as well as the marginal PDFs of the corresponding coefficients at the ranges $\eta = 0.5, 5, 10$ km.

as described in several studies (Charous and Lermusiaux, 2023; Feppon and Lermusiaux, 2018b; Lermusiaux, 2007; Lin, 2020; Sapsis and Lermusiaux, 2012).

IV. UNCERTAIN UP-SLOPING WEDGE (UW)

The third test case extends the deterministic range-dependent 2D up-sloping wedge (UW) benchmark with penetrable fluid bottom (Jensen and Ferla, 1990) to a stochastic UW with a probabilistic bathymetric slope of large uncertainty. A point sound source is located at depth $Z_s = 100$ m and range $\eta = 0$ and emits at a harmonic frequency $f = 25$ Hz. The deterministic waveguide is an isospeed sound channel with $c_w = 1500$ m/s, $\rho_w = 1000\,\mathrm{kg/m^3}$, and $\alpha_w = 0$. The uncertain seafloor slope is a random variable characterized by its depth intersect Z_w at the final range of $R = 4$ km, with $Z_w \sim U[0, 200]$ m. The bottom medium beneath the stochastic slope is a penetrable fluid half-space with $c_b = 1700$ m/s, $\rho_b = 1000\,\mathrm{kg/m^3}$, and $\alpha_b = 1\,\mathrm{dB}/\lambda$. The reference sound speed is $c_0 = 1500$ m/s. A schematic of the test case is provided in Fig. 15 where some sample realizations of the seafloor slope are also illustrated in white.

A. DO-NAPE input n^2_{eff} decomposition

The uncertainty in the seafloor slope renders the sound speed and attenuation fields both stochastic and range-dependent, which in turn leads to a stochastic range-

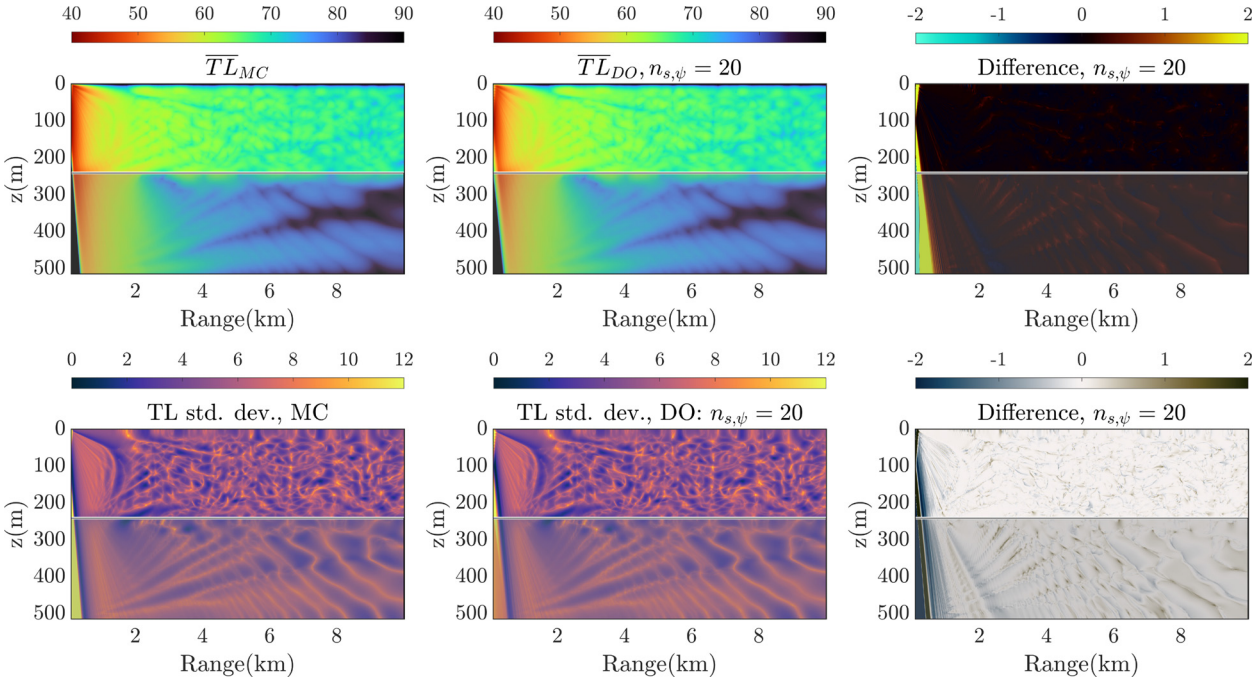

FIG. 13. (Color online) Uncertain HI: Comparisons of the MC (left) and DO-NAPE (middle) solutions for the mean (top row, in dB) and standard deviation (bottom row, in dB^2) fields of TL.

dependent squared effective index of refraction $n^2_{eff}(z, \eta; \xi)$. The input DO decomposition of n^2_{eff} is therefore range-dependent. Thresholding the singular values obtained when taking the SVD of the n^2_{eff} realizations field led to choosing $n_{s,n^2} = 6$. Figure 16 shows the mean and dominant four (out of six) modes and stochastic coefficients of n^2_{eff}.

B. DO-NAPE solutions

The DO-NAPEs were initialized using the deterministic source procedure of case 2, Sec. III E 3 of Part I (Ali and Lermusiaux, 2024). They were solved for the pressure envelope ψ using $n_{s,\psi} = 9$ stochastic modes and $n_r = 2000$ coefficient realizations. In other words, a single DO-NAPE simulation is analogous to running 2000 MC realizations: results including mean, statistics, and realization fields are very close (shown later). Inserting the values $\kappa = 1$, $n_r = 2000$, $n_{s,n^2} = 6$, and $n_{s,\psi} = 9$ in the cost ratio Eq. (A5), we obtain the computational saving of $\text{Cost}_{MC}/\text{Cost}_{DO} \sim 31.7$. We note that this saving ratio of the DO-NAPE framework increases further if the number of realizations is increased.

From the DO-NAPE prediction of the stochastic ψ field, the global SVD approach described in Sec. III G in Part I (Ali and Lermusiaux, 2024) and summarized in the

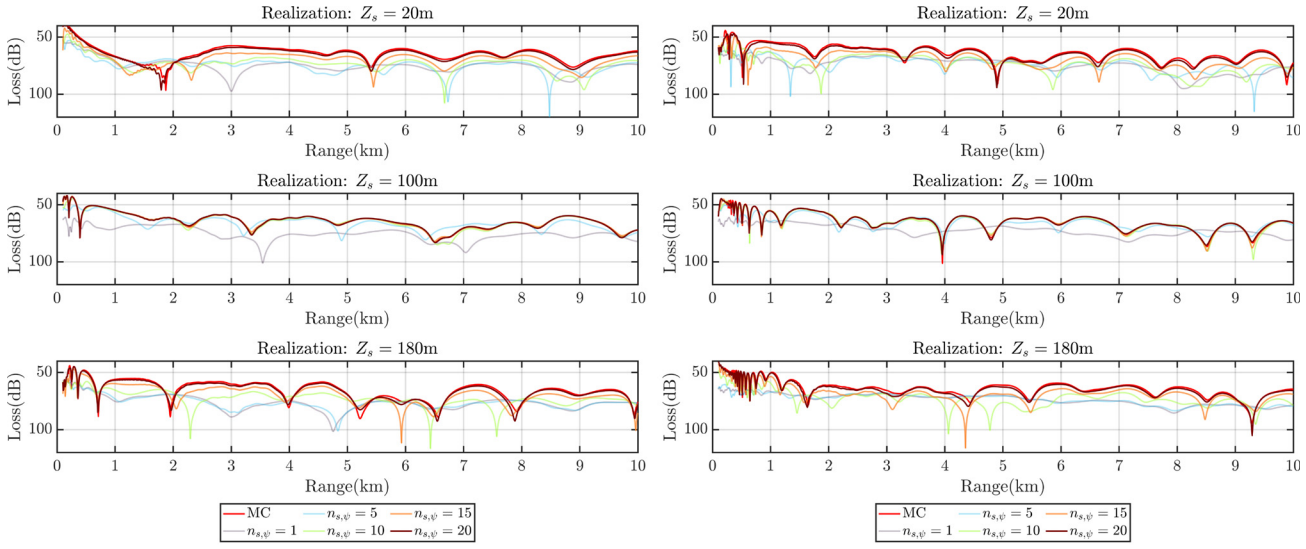

(a) $Z_{receiver} = 30\ m$ (b) $Z_{receiver} = 190\ m$

FIG. 14. (Color online) Uncertain HI: Comparisons of the MC TL (in dB) solution to DO-NAPE TL solutions ($n_{s,\psi} = 1, 5, 10, 15, 20$) for the sample source depth realizations $Z_s = 20, 100, 180$ m, at two receiver locations: (a) TL at $Z_{receiver} = 30$ m and (b) TL at $Z_{receiver} = 190$ m.

https://doi.org/10.1121/10.0024474

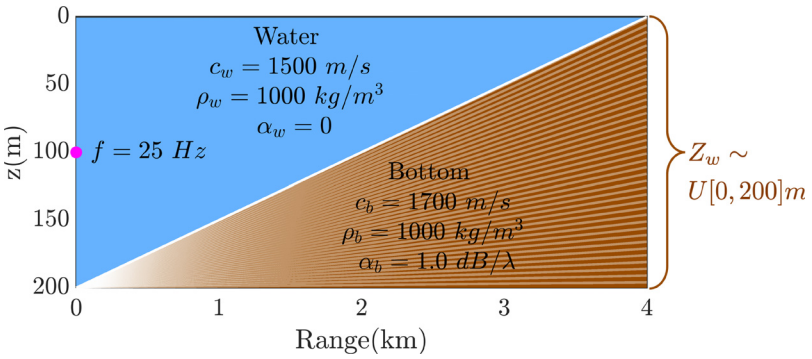

FIG. 15. (Color online) Uncertain UW: Schematic. A point sound source is located at depth $Z_s = 100\,m$ and range $\eta = 0$ and emits at a harmonic frequency $f = 25$ Hz. The uncertain seafloor slope is a random variable characterized by its depth intersect Z_w at the final range of $R = 4$ km, with uniform PDF, i.e., $Z_w \sim U[0, 200]$ m. Some sample realizations of the seafloor slope are illustrated in white. Other parameters are deterministic as given in the schematic and described in the text.

Appendix was used to obtain a global DO decomposition for TL. In order to illustrate the nonlinear effects in this UW case, Fig. 17 compares the mean of the TL computed from the DO-NAPE solution to a deterministic run where the slope intersects the final range at the mean depth $Z = \overline{Z_w} = 100$ m. The mean TL solution is found to be significantly different from the deterministic solution for the mean bathymetric slope, highlighting the need for a probabilistic nonlinear simulation.

In addition to the mean solution, the four dominant DO-NAPE modes and stochastic coefficients of TL are shown in Fig. 18. The non-Gaussian statistics in this case can be observed in the multimodal PDFs of the coefficients. In addition, the DO-NAPE modal energies are found to be

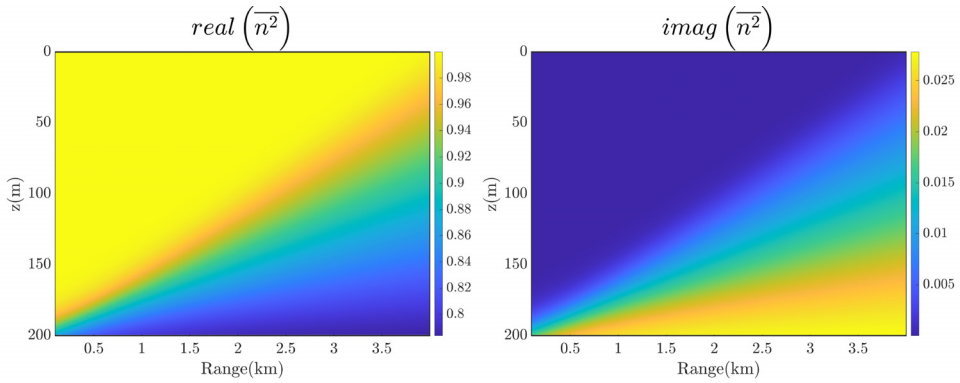

(a) H DO Mean

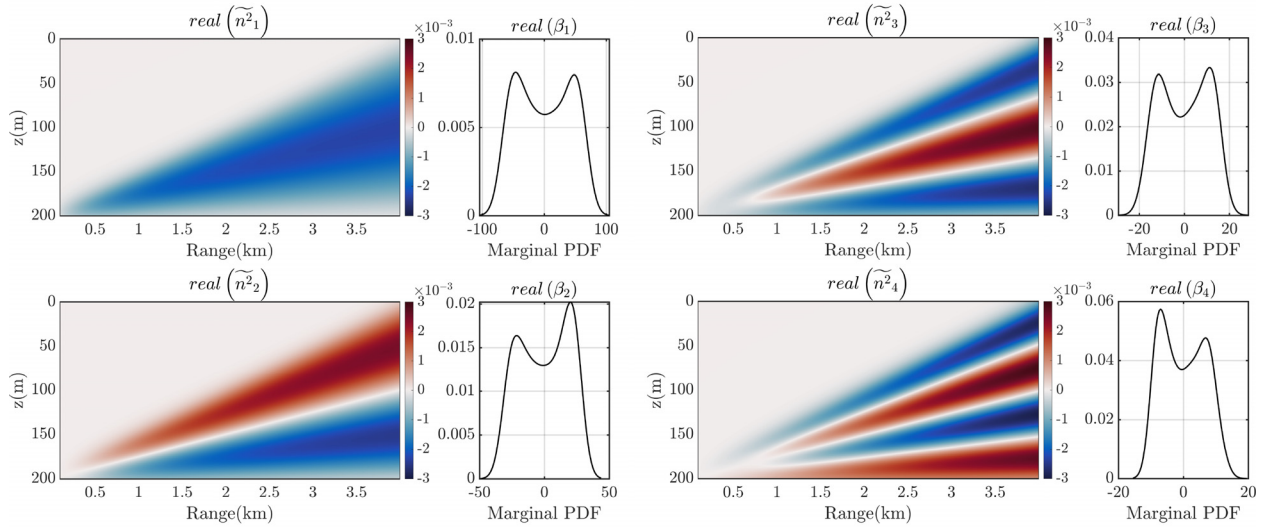

(b) H DO Modes and Coefficients

FIG. 16. (Color online) Uncertain UW: Input DO decomposition of n^2_{eff}. (a) Mean and (b) Dominant four modes along with the marginal PDFs of their coefficients.

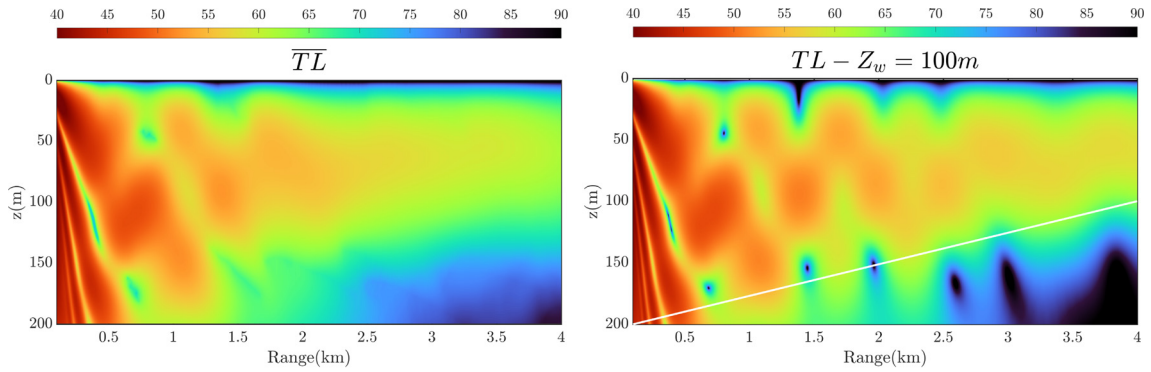

(a) $\overline{TL}_{DO}$ (b) TL at $\overline{Z_w} = 100\ m$

FIG. 17. (Color online) Uncertain UW: Comparison of the mean TL (in dB) solution obtained using DO-NAPE to the deterministic TL solution for the mean slope, i.e., for the bathymetry intersecting the final range at the mean depth $\overline{Z_w} = 100$ m.

lower at short ranges where the sound waves had fewer bounces off the uncertain slope.

C. DO-NAPE validation

To validate the DO solution, the corresponding MC solutions were computed by solving the range-dependent deterministic NAPE for each of the n_r realizations of the slope intersect. The comparison results are first illustrated in Fig. 19 here the TL solutions are compared for three sample slope realizations, $Z_w = 0$, 100, and 200 m. The first row shows the diagram of the 3 sample cases with a dashed line corresponding to the receiver location $Z_r = 100$ m. Comparisons of TL at this receiver are shown in the second row for increasing dimensions of the stochastic subspace $n_{s,\psi} = 1, 3, 5, 7, 8, 9$, along with the MC solution in red. The TL computed by the DO-NAPE solution with $n_{s,\psi} = 9$ are nearly identical to the TL computed by the MC method. The third row shows heatmaps of the TL MC solutions with the white line indicating the seafloor slope. Comparing these solutions to the TL realizations computed from DO-NAPE in the fourth row, the errors shown in the fifth row are found to be negligible highlighting the accuracy of the DO framework. The range dependencies, the amplitudes, and the phases including the nulls are all captured, even though the DO-NAPEs compute all the 2000 realizations at once, at a much-reduced cost.

Matching MC realizations is a strong and often difficult validation test for any stochastic modeling method. A complementary test requires matching the corresponding PDFs, in this case, the PDF of TL. Figure 20 illustrates the results of these two realization and PDF tests for TL at two receiver locations, $Z_{receiver} = 50, 100$ m. The first column in Fig. 20(a) shows the mean (solid line) and min-max band (shaded area around the mean that highlights realizations the furthest from the mean) of TL at $Z_{receiver} = 50$ m, i.e., the band formed by computing all the minimum and maximum realizations of TL due to the seafloor slope uncertainty, computed from the MC (red) and DO-NAPE (blue) solutions. The remaining panels show the PDFs of the TL realizations at the receiver location for ranges $\eta = 1, 2, 3, 4$ km. The DO-NAPE min-max band and PDFs show good

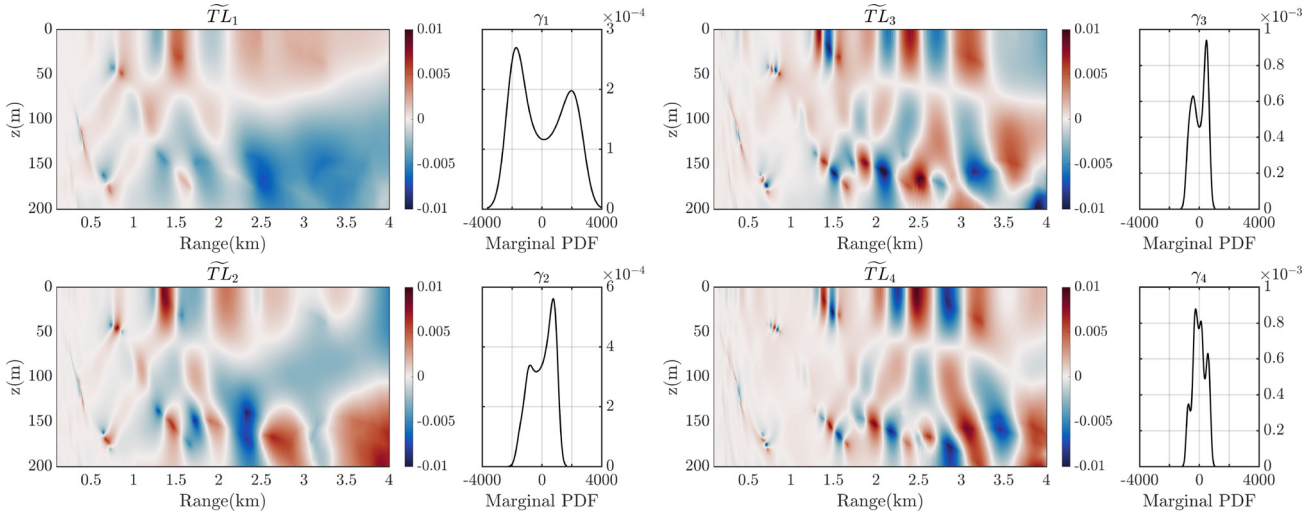

FIG. 18. (Color online) Uncertain UW: Four dominant stochastic DO-NAPE TL modes (non-dimensional) and coefficients (in dB).

https://doi.org/10.1121/10.0024474

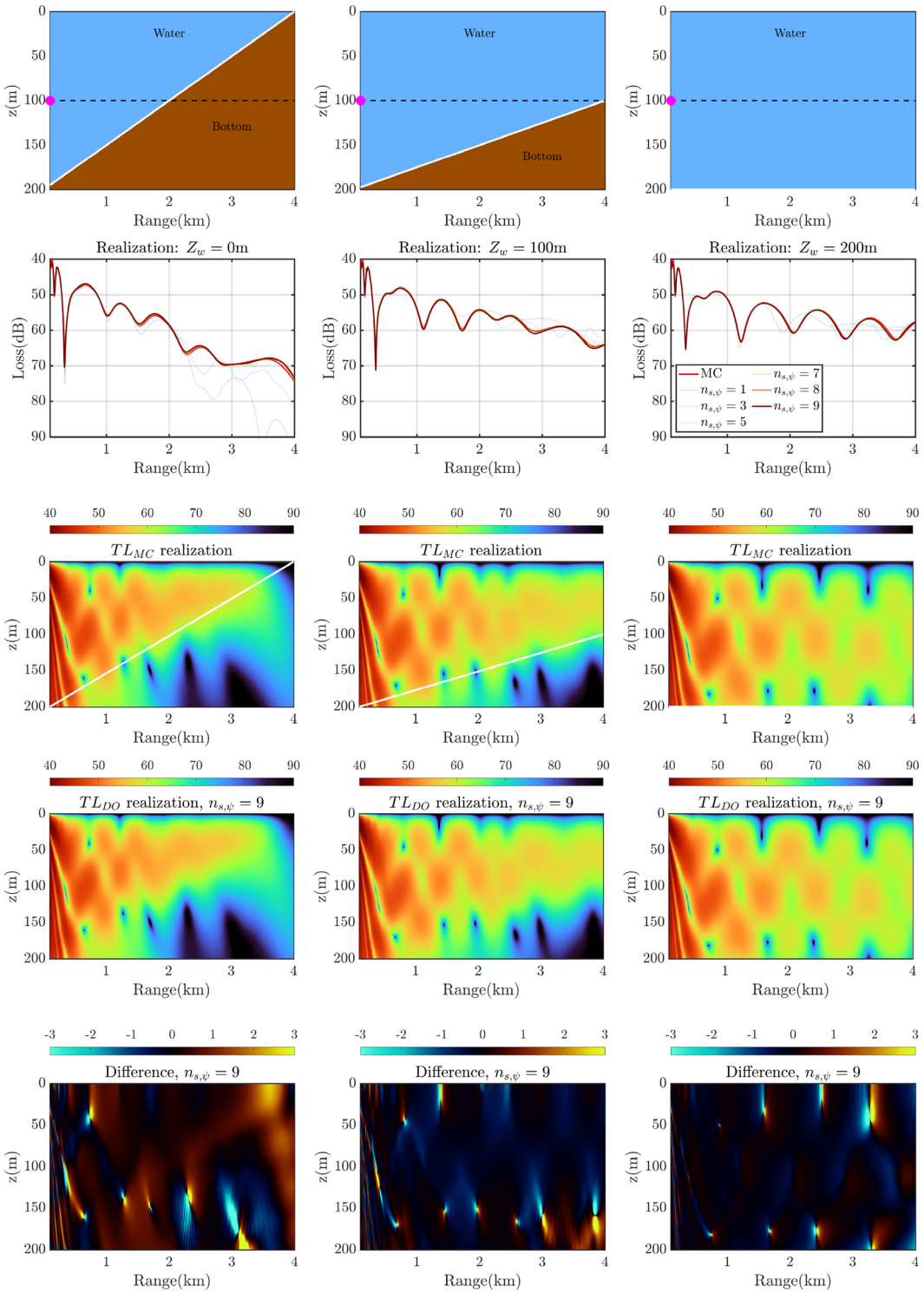

FIG. 19. (Color online) Uncertain UW: Comparisons of TL (in dB) computed by DO-NAPE and by MC, for three sample realizations of the slope intersect: $Z_w = 0$ m (first column), $Z_w = 100$ m (second column), and $Z_w = 200$ m (third column).

agreement with the corresponding MC solutions. The same conclusions hold for the results at $Z_{receiver} = 100$ m shown in Fig. 20(b), where the DO-NAPE min-max band and PDFs of TL match the multimodal distributions of the MC solutions relatively well, at both short and long ranges. Note that both the MC and DO-NAPE are approximations. In some cases, as the range increases, if the MC does not sample the probability space adequately anymore, the DO-NAPE solution can be more accurate than MC for the same number of realizations or even converge faster than MC toward the true stochastic solution. This is in part because the DO-NAPE adapts in range toward the regions of the state space where dominant uncertainties occur.

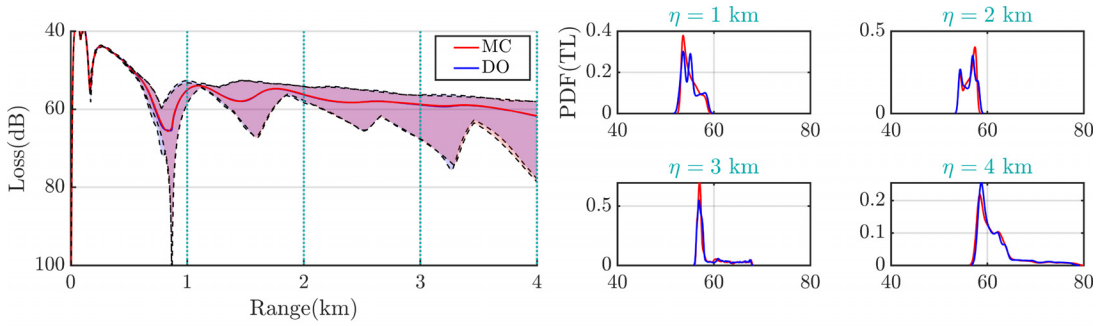

(a) $Z_{receiver} = 50$ m

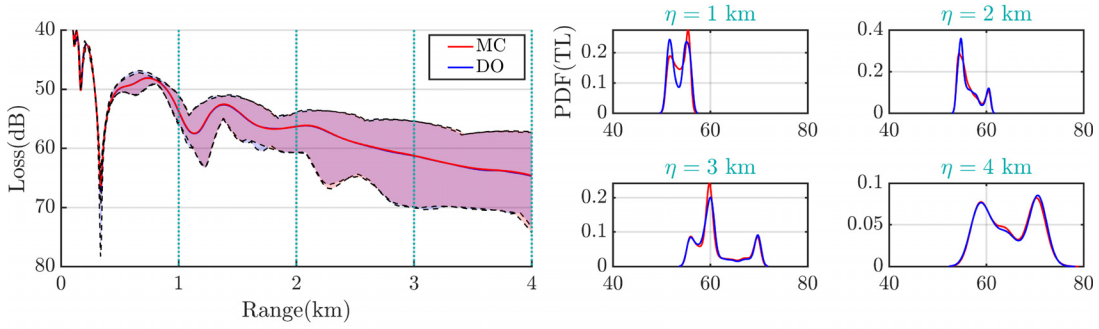

(b) $Z_{receiver} = 100$ m

FIG. 20. (Color online) Uncertain UW: Comparisons of the mean, min-max band (band of minimum and maximum values across all realizations), and PDFs of TL (in dB) computed from the DO-NAPE solution and from a MC ensemble with 2000 realizations. The TLs shown correspond to receivers located at (a): $Z_{receiver} = 50$ m and (b): $Z_{receiver} = 100$ m.

V. SUMMARY AND CONCLUSIONS

In Part II of this two-part paper, the DO-NAPEs are applied and their properties are analyzed for three new 2D stochastic canonical test cases: (1) an uncertain range-independent PW with stochastic sound speed, (2) an uncertain range-independent HI problem with stochastic source depth, and (3) an uncertain range-dependent UW problem with stochastic bathymetry. Results showed that the DO-NAPEs can predict accurate stochastic responses to complex input probability distributions (uniform, multi-modal, large deviations, etc.) in sound speed, bathymetry, and source location. The first test case was utilized to illustrate the DO-NAPE methodology and to show and verify that the DO-NAPE solutions match an ensemble of ground-truth deterministic analytical solutions. The DO-NAPE pressure, phase, TL fields, and their amplitudes, nulls, and other features, were found to be accurate and to converge as the dimension of the stochastic subspace and the number of samples increased. In the second case, the stochastic source depth in a range-independent environment was shown to lead to non-Gaussian and strongly range-dependent statistics captured by the DO-NAPE coefficients. The DO-NAPE stochastic TL solutions were indeed confirmed to converge statistically, for the first (mean) and second-order (standard deviation) terms but also the full PDFs, as well as deterministically at the realization level shown by comparison of reconstructed DO-NAPE realizations with direct deterministic MC solutions. The third test case included more complex sound speed and bathymetry range dependencies. The range-dynamic properties of the DO-NAPEs were illustrated and the DO-NAPE solution matched the TL fields and non-Gaussian PDFs obtained from an ensemble of deterministic MC runs with 2000 realizations. These results highlight the capabilities of the DO-PEs in contrast to other methods.

Importantly, in all three test cases, none of the mean, DO modes, and DO coefficients, are predefined. Instead, they are governed by the stochastic DO-NAPEs [Eq. (A4)] derived directly from the stochastic NAPE and adapt in range to the dominant uncertainties, as highlighted by Figs. 4, 5, 12, 17, and 18. The DO-NAPEs are the instantaneously optimal low-rank approximation of the range-dynamics of the matrix of all the realizations of ψ (Feppon and Lermusiaux, 2018a,b). A consequence of this property is demonstrated by the excellent matching of individual realizations, statistics, and PDFs of the phase and TL (Figs. 9, 13, 14, 19, and 20), even after the stochastic numerical errors (spatial discretization, sampling, and retraction errors) of the discrete DO-NAPEs are compounded over range. Finally, the significant computational savings of the DO-NAPEs over direct MC methods were also highlighted, both in numerical cost estimates and in actual simulations, which in the three test cases shown in this Part II paper reach factors of about 30 to 250 in computational speedup.

ACKNOWLEDGMENTS

We thank the members of our MSEAS group. We are grateful to the Office of Naval Research for research support

under grants N00014-19-1-2664 (Task Force Ocean: DEEP-AI) and N00014-19-1-2693 (IN-BDA) to the Massachusetts Institute of Technology. We thank the editor and the reviewers for their useful comments.

AUTHOR DECLARATIONS

Conflict of Interest

The authors have no conflict to disclose.

DATA AVAILABILITY

The data that support the findings of this study are available from the corresponding author upon reasonable request.

APPENDIX: DO-NAPE NOTATION AND EQUATIONS

We summarize the notation, main equations, computational costs, and DO TL post-processing developed in Part I (Ali and Lermusiaux, 2024) and utilized in this Part II.

1. Notation and equations

In the test cases of Part II, we consider stochastic acoustic propagation along 2D slices in uncertain multilayered ocean environments. We denote the spatial position by $\boldsymbol{x} = (z, \eta)$ where z is the depth measured from the surface and $\eta \in (0, R]$ the position in the range direction with R referring to the total propagation range. The uncertain multilayered media are characterized by stochastic space-varying medium density $\rho(z, \eta; \xi)$, sound speed $c(z, \eta; \xi)$, and attenuation $a(z, \eta; \xi)$. These space-varying fields are stochastic and indexed by the stochastic parameter ξ, which represents an event in the stochastic event space Ξ. Altogether, they define the stochastic squared effective index of refraction,

$$n^2_{eff}(z,\eta;\xi) = \left(\frac{c_0}{c}\right)^2 \left(1 + i\frac{a}{27.29}\right) + \frac{1}{2k_0^2}\left(\frac{1}{\rho}\frac{\partial^2\rho}{\partial z^2} - \frac{3}{2\rho^2}\left(\frac{\partial\rho}{\partial z}\right)^2\right), \tag{A1}$$

where $k_0 = \omega/c_0$ is a reference wavenumber, $\omega = 2\pi f$ is the source angular frequency, and c_0 is a reference sound speed.

Under the NAPE approximation, the stochastic PDE describing the range-evolution of the outgoing envelope function $\boldsymbol{\psi}$ for the stochastic acoustic pressure reduces to

$$\frac{\partial\boldsymbol{\psi}(z,\eta;\xi)}{\partial\eta} = \left\{\frac{i}{2k_0}\frac{\partial^2}{\partial z^2} + \frac{ik_0}{2}\left(n^2_{eff}(z,\eta;\xi) - 1\right)\right\}\boldsymbol{\psi}(z,\eta;\xi), \quad z \in [0, Z_{max} + D], \eta \in (0, R], \xi \in \Xi, \tag{A2}$$

where Z_{max} is the total depth of the environment including both the water depth and the depths of the sediment layers, D is the thickness of the artificial absorption layer, and R is the total propagation range.

The stochastic fields in Eq. (A2), the input index of refraction field $n^2_{eff}(z, \eta; \xi)$ and unknown output complex envelope pressure field $\boldsymbol{\psi}(z, \eta; \xi)$, are decomposed in terms of their range-dynamic Karhunen-Loève (DO) expansions,

$$n^2_{eff}(z,\eta;\xi) \approx \left(n^2_{eff}\right)_{DO} = \overline{n^2}(z,\eta) + \sum_{l=1}^{n_{s,n^2}} \widetilde{n^2}_l(z,\eta)\beta_l(\eta;\xi), \tag{A3a}$$

$$\boldsymbol{\psi}(z,\eta;\xi) \approx \boldsymbol{\psi}_{DO} = \bar{\boldsymbol{\psi}}(z,\eta) + \sum_{i=1}^{n_{s,\psi}} \widetilde{\boldsymbol{\psi}}_i(z,\eta)\alpha_i(\eta;\xi)\,. \tag{A3b}$$

In Eq. (A3), $\overline{n^2}(z, \eta)$ and $\bar{\boldsymbol{\psi}}(z, \eta)$ are statistical mean fields for the index of refraction and complex pressure, respectively. The fields $\widetilde{n^2}_l(z, \eta)$, $\forall l = 1, \ldots, n_{s,n^2}$, and $\widetilde{\boldsymbol{\psi}}_i(z, \eta)$, $\forall i = 1, \ldots, n_{s,\psi}$, are DO modes, each set defining a range-dynamic basis, orthonormal in the transverse spatial space (z) by construction. The DO stochastic coefficients $\beta_l(\eta; \xi), \forall l = 1, \ldots, n_{s,n^2}$, and $\alpha_i(\eta; \xi), \forall i = 1, \ldots, n_{s,\psi}$, are each zero-mean stochastic processes that can represent complex range-dependent uncertainties in the squared effective index of refraction and acoustic fields, respectively. In our applications, the right-hand-side of Eq. (A3a) is defined by each test case but, in general, would come from a stochastic ocean modeling system (Lermusiaux, 1999, 2007; Lermusiaux *et al.*, 2020; Lermusiaux and Robinson, 1999; Robinson *et al.*, 2002). Most importantly in this work, none of the acoustic pressure mean $\bar{\boldsymbol{\psi}}(z, \eta)$, DO modes $\widetilde{\boldsymbol{\psi}}_i(z, \eta)$, and DO coefficients $\alpha_i(\eta; \xi)$, are predefined. Instead, they are governed by the following stochastic DO-NAPEs (Ali and Lermusiaux, 2024):

$$\frac{\partial\bar{\boldsymbol{\psi}}(z,\eta)}{\partial\eta} = \frac{i}{2k_0}\frac{\partial^2}{\partial z^2}\bar{\boldsymbol{\psi}} + \frac{ik_0}{2}\bar{\boldsymbol{\psi}}(\overline{n^2} - 1) + \sum_{i=1}^{n_{s,\psi}}\sum_{l=1}^{n_{s,n^2}} \frac{ik_0}{2} C_{\alpha_i\beta_l}\widetilde{n^2}_l\widetilde{\boldsymbol{\psi}}_i\,, \tag{A4a}$$

$$\frac{\partial\widetilde{\boldsymbol{\psi}}_i(z,\eta)}{\partial\eta} = Q_i - \sum_{j=1}^{n_{s,\psi}} \langle Q_i, \widetilde{\boldsymbol{\psi}}_j\rangle\widetilde{\boldsymbol{\psi}}_j, \quad \forall i = 1, \ldots, n_{s,\psi}, \tag{A4b}$$

where

$$\begin{aligned} Q_i = {} & \frac{i}{2k_0}\frac{\partial^2}{\partial z^2}\widetilde{\boldsymbol{\psi}}_i + \frac{ik_0}{2}(\overline{n^2} - 1)\widetilde{\boldsymbol{\psi}}_i \\ & + \sum_{n=1}^{n_{s,\psi}} C^{-1}_{\alpha_n\alpha_i}\left[\sum_{l=1}^{n_{s,n^2}} C_{\alpha_n\beta_l}\frac{ik_0}{2}\widetilde{n^2}_l\bar{\boldsymbol{\psi}}\right. \\ & \left. + \sum_{k=1}^{n_{s,\psi}}\sum_{l=1}^{n_{s,n^2}} E^{\xi}[\alpha_n\beta_l\alpha_k]\frac{ik_0}{2}\widetilde{n^2}_l\widetilde{\boldsymbol{\psi}}_k\right], \\ \frac{d\alpha_i(\eta;\xi)}{d\eta} = {} & \sum_{k=1}^{n_{s,\psi}}\alpha_k\left\langle\frac{i}{2k_0}\frac{\partial^2}{\partial z^2}\widetilde{\boldsymbol{\psi}}_k, \widetilde{\boldsymbol{\psi}}_i\right\rangle \\ & + \sum_{k=1}^{n_{s,\psi}}\alpha_k\left\langle\frac{ik_0}{2}(\overline{n^2} - 1)\widetilde{\boldsymbol{\psi}}_k, \widetilde{\boldsymbol{\psi}}_i\right\rangle \\ & + \sum_{l=1}^{n_{s,n^2}}\beta_l\left\langle\frac{ik_0}{2}\widetilde{n^2}_l\bar{\boldsymbol{\psi}}, \widetilde{\boldsymbol{\psi}}_i\right\rangle \\ & + \sum_{k=1}^{n_{s,\psi}}\sum_{l=1}^{n_{s,n^2}}(\alpha_k\beta_l - C_{\alpha_k\beta_l})\left\langle\frac{ik_0}{2}\widetilde{n^2}_l\widetilde{\boldsymbol{\psi}}_k, \widetilde{\boldsymbol{\psi}}_i\right\rangle, \\ & \forall i = 1, \ldots, n_{s,\psi}\,, \end{aligned} \tag{A4c}$$

where C denotes a range-varying covariance matrix between two stochastic processes. For instance, $C_{\alpha_i\beta_l}(\eta) = E^{\xi}[\alpha_i(\eta;\xi) \times \beta_l(\eta;\xi)]$. The DO-NAPEs [Eq. (A4)] are directly derived from the stochastic NAPE [Eq. (A2)] by applying expectation and projection operators onto the DO modes and coefficients. Their solutions provide predictions of the stochastic acoustic field $\boldsymbol{\psi}(z,\eta;\xi)$, where $z \in [0, Z_{max}+D]$ and $\eta \in (0,R]$, for all realizations $\xi \in \Xi$.

The DO-NAPEs [Eq. (A4)] are subject to the DO stochastic ICs (Sec. III B 1 of Part I) and BCs (Sec. III B 2 of Part I). They are solved numerically using schemes described in Sec. III E of Part I.

2. Computational costs

As developed in Sec. III F of Part I (Ali and Lermusiaux, 2024), significant computational savings are achieved using DO-PEs. With the present DO-NAPEs for 2D stochastic propagation, the ratio of the number of operations needed for direct MC simulations of n_r deterministic realizations to that needed for DO-NAPEs is of the order,

$$\frac{\text{Cost}_{MC}}{\text{Cost}_{DO}} \sim \frac{n_r N_{\boldsymbol{x}_\perp}^{\kappa-1}}{n_{s,\boldsymbol{\psi}} N_{\boldsymbol{x}_\perp}^{\kappa-1} + n_{s,n^2} n_{s,\boldsymbol{\psi}}} \overset{\kappa=1}{=} \frac{n_r}{n_{s,\boldsymbol{\psi}} + n_{s,n^2} n_{s,\boldsymbol{\psi}}}, \tag{A5}$$

where $\kappa = 1$ corresponds to the case of one-dimensional (1D) transverse physical space ($D \equiv z$) with a 2nd order central differencing scheme considered in the applications in this Part II.

In addition to the previously noted computational speedup ratio, memory savings at each range step can also be achieved by the DO-NAPEs. These memory savings can be on the order of

$$\frac{\text{Memory}_{MC}}{\text{Memory}_{DO}} \sim \frac{n_r N_z}{n_{s,\boldsymbol{\psi}}(n_r + N_z)}, \tag{A6}$$

where N_z is the number of finite volume grid points used in the depth (z) dimension.

3. DO TL post-processing

As discussed in Sec. III G of Part I, once the DO-NAPEs [Eq. (A4)] are solved for the complex-valued mean field $\bar{\boldsymbol{\psi}}(z,\eta)$, modes $\widetilde{\boldsymbol{\psi}}_{i=1,\ldots,n_{s,\boldsymbol{\psi}}}(z,\eta)$, and stochastic coefficients $\alpha_{i=1,\ldots,n_{s,\boldsymbol{\psi}}}(\eta;\xi)$, the TL DO solution can be reconstructed as a postprocessing step using

$$\begin{aligned} TL(z,\eta;\xi) &= -20\log_{10}\left|\frac{\boldsymbol{\psi}(z,\eta;\xi)}{\sqrt{\eta}}\right| \\ &= -20\log_{10}\left|\frac{\bar{\boldsymbol{\psi}} + \sum_{i=1}^{n_{s,\boldsymbol{\psi}}} \widetilde{\boldsymbol{\psi}}_i \alpha_i}{\sqrt{\eta}}\right|, \end{aligned} \tag{A7}$$

where the $1/\sqrt{\eta}$ term is added to account for cylindrical spreading (Jensen *et al.*, 2011).

Out of the two approaches (range-dependent SVD vs global SVD) presented in Part I, the DO TL results shown here in Part II rely on the global SVD approach. The DO decomposition of the stochastic 2D TL field is then computed in one shot by taking the SVD of the 2D realization field $TL(z,\eta;\xi)$. This approach yields the mean field $\overline{TL}(z,\eta)$ (units: dB), modes $\widetilde{TL}_{k=1,\ldots,n_{s,TL}}(z,\eta)$ (non-dimensional), and stochastic coefficients $\gamma_{k=1,\ldots,n_{s,TL}}(\xi)$ (range-independent, units: dB).

Ali, W. H., and Lermusiaux, P. F. J. (**2024**). "Dynamically orthogonal narrow-angle parabolic equations for stochastic underwater sound propagation. Part I: Theory and schemes," J. Acoust. Soc. Am. **155**(1), 640–655.

Branicki, M., and Majda, A. J. (**2013**). "Fundamental limitations of polynomial chaos for uncertainty quantification in systems with intermittent instabilities," Commun. Math. Sci. **11**(1), 55–103.

Charous, A., and Lermusiaux, P. F. J. (**2023**). "Stable rank-adaptive dynamically orthogonal Runge–Kutta schemes," SIAM J. Sci. Comput. (in press).

Feppon, F., and Lermusiaux, P. F. J. (**2018a**). "A geometric approach to dynamical model-order reduction," SIAM J. Matrix Anal. Appl. **39**(1), 510–538.

Feppon, F., and Lermusiaux, P. F. J. (**2018b**). "Dynamically orthogonal numerical schemes for efficient stochastic advection and Lagrangian transport," SIAM Rev. **60**(3), 595–625.

Jensen, F. B., and Ferla, C. M. (**1990**). "Numerical solutions of range-dependent benchmark problems in ocean acoustics," J. Acoust. Soc. Am. **87**(4), 1499–1510.

Jensen, F. B., Kuperman, W. A., Porter, M. B., and Schmidt, H. (**2011**). *Computational Ocean Acoustics* (Springer Science & Business Media, New York).

Lee, D., and McDaniel, S. (**1988**). "Chapter 8—Representative test examples," in *Ocean Acoustic Propagation by Finite Difference Methods*, edited by D. Lee and S. McDaniel (Pergamon, Amsterdam), pp. 369–383.

Lermusiaux, P. F. J. (**1999**). "Data assimilation via error subspace statistical estimation, Part II: Mid-Atlantic bight shelfbreak front simulations, and ESSE validation," Mon. Weather Rev. **127**(7), 1408–1432.

Lermusiaux, P. F. J. (**2007**). "Adaptive modeling, adaptive data assimilation and adaptive sampling," Phys. D **230**(1), 172–196.

Lermusiaux, P. F. J., Mirabito, C., Haley, P. J., Jr., Ali, W. H., Gupta, A., Jana, S., Dorfman, E., Laferriere, A., Kofford, A., Shepard, G., Goldsmith, M., Heaney, K., Coelho, E., Boyle, J., Murray, J., Freitag, L., and Morozov, A. (**2020**). "Real-time probabilistic coupled ocean physics-acoustics forecasting and data assimilation for underwater GPS," in *Proceedings of Oceans 2020*, October 5–14, Virtual, pp. 1–9.

Lermusiaux, P. F. J., and Robinson, A. R. (**1999**). "Data assimilation via error subspace statistical estimation, Part I: Theory and schemes," Mon. Weather Rev. **127**(7), 1385–1407.

Lin, J. (**2020**). "Bayesian learning for high-dimensional nonlinear systems: Methodologies, numerics and applications to fluid flows," Ph.D. thesis, Massachusetts Institute of Technology, Cambridge, MA.

Pekeris, C. L. (**1948**). "Theory of propagation of explosive sound in shallow water," in *Propagation of Sound in the Ocean* (Geological Society of America, Boulder, CO).

Robinson, A. R., Abbot, P., Lermusiaux, P. F. J., and Dillman, L. (**2002**). "Transfer of uncertainties through physical-acoustical-sonar end-to-end systems: A conceptual basis," in *Acoustic Variability, 2002*, edited by N. G. Pace and F. B. Jensen (Kluwer Academic Press, Philadelphia, PA), pp. 603–610.

Sapsis, T. P., and Lermusiaux, P. F. J. (**2012**). "Dynamical criteria for the evolution of the stochastic dimensionality in flows with uncertainty," Phys. D **241**(1), 60–76.

Schmidt, H., and Jensen, F. B. (**1985**). "A full wave solution for propagation in multilayered viscoelastic media with application to Gaussian beam reflection at fluid–solid interfaces," J. Acoust. Soc. Am. **77**(3), 813–825.

Ueckermann, M. P., Lermusiaux, P. F. J., and Sapsis, T. P. (**2013**). "Numerical schemes for dynamically orthogonal equations of stochastic fluid and ocean flows," J. Comput. Phys. **233**, 272–294.